

Flow structure and acoustics of supersonic jets from conical convergent-divergent nozzles

D. Munday,¹ E. Gutmark,¹ J. Liu,² and K. Kailasanath²

¹University of Cincinnati, Cincinnati, Ohio 45221, USA

²Naval Research Laboratory, Washington, D.C. 20375, USA

(Received 4 April 2011; accepted 22 August 2011; published online 22 November 2011)

Conical convergent-divergent (CCD) nozzles represent an important category of supersonic jet-engine nozzles which require variable throat areas and variable exit areas to adapt to a range of operating conditions. CCD nozzles with design Mach numbers of 1.3, 1.5, and 1.65 are examined experimentally over a range of fully expanded Mach numbers from 1.22 to 1.71. The characteristics of the flow and acoustic fields from these nozzles are explored. Shadowgraph, Particle Image Velocimetry, far-field and near-field acoustic surveys are presented. Results of a Monotonically Integrated Large Eddy Simulation are presented for the Mach 1.5 nozzle at an underexpanded condition. The agreement between simulations and measurements is excellent. It is shown that these nozzles differ from traditional smoothly contoured method-of-characteristics nozzles in that they never achieve a shock free condition. Furthermore it is shown that these nozzles produce a “double diamond” pattern in which two sets of shock diamonds are generated with an axial displacement between them. The cause of this phenomenon is explored. It is further shown that as a consequence they are never free from shock-associated noise even when operated at perfect expansion. In spite of this difference, it is found that CCD nozzles behave like traditional convergent-divergent nozzles in that they produce the same shock-cell size, broadband shock-associated noise peak frequency, and screech frequency as traditional convergent-divergent nozzles. The apparent source regions for mixing noise, broadband shock associated noise and screech are all similar to those from traditional convergent-divergent nozzles. © 2011 American Institute of Physics. [doi:10.1063/1.3657824]

I. INTRODUCTION

Since the early twentieth century, it has been recognized that convergent-divergent nozzles, when operated off-design, generate semi-periodic shock diamonds as shocks and Prandtl-Meyer fans alternate in the jet plume.¹ For traditional smoothly contoured convergent-divergent (C-D) nozzles, designed for isentropic expansion and parallel exit flow, matching the exit pressure to the ambient pressure produces a supersonic jet which is shock free. Such a condition, with pressures matched at the exit, is referred to as the nozzle’s design condition.

In order to attain a shock free design condition, traditional convergent-divergent nozzles (C-D nozzles) employed in most laboratory studies have special design features. The nozzle throats are smooth with large-radius curves. Isentropic expansion in the divergent section is achieved by designing the nozzle shape using the method of characteristics or by numerical simulation. The contours of these traditional nozzles have zero slope at the exit so that they produce parallel exit flows. Such contours present a practical problem for the designer of a high-performance jet engine exhaust nozzle. Since aircraft must operate over a range of atmospheric conditions and power levels, a variable-geometry nozzle is generally required. The throat area must be changed to attain the desired mass flows and the area ratio between throat and exit must be changed to adapt to conditions and thrust requirements.

While it is possible to design a variable geometry nozzle with smooth contours, such a nozzle would be complex and heavy. What is commonly done in high-performance jet aircraft exhausts is to employ a variable geometry nozzle with flat plates in the convergent section and flat plates in the divergent section with seals between so that the plates make a cross section that is polyhedral and approximates a circle. The plates are hinged between the convergent and divergent sections making a relatively sharp corner at the throat. Such a nozzle trades a reduction in nozzle efficiency for a reduction in weight and complexity. The conical C-D (CCD) nozzles employed in this study match the stream-wise contours of the real engine nozzles. The cross sections are circular and thus the convergent and divergent sections are conical.

Like the variable geometry nozzles used in actual practice, these conical nozzles do not approach a cylindrical shape at the exit, so unless the flow is massively separated they can never emit parallel flow. Turning of the flow at the exit will be necessary and this will produce shocks or Prandtl-Meyer waves in the jet even at the design condition when there is no pressure mismatch. It will be shown that these nozzles are not shock free at or near their design conditions. It will also be shown that these nozzles generate a second set of shock diamonds superimposed on the first, generating a double-diamond pattern. This second set of shock diamonds has its origin at the sharp nozzle throat. The presence or absence of shocks in the jet plume has a significant effect on the acoustic emissions of the jet.

Report Documentation Page

Form Approved
OMB No. 0704-0188

Public reporting burden for the collection of information is estimated to average 1 hour per response, including the time for reviewing instructions, searching existing data sources, gathering and maintaining the data needed, and completing and reviewing the collection of information. Send comments regarding this burden estimate or any other aspect of this collection of information, including suggestions for reducing this burden, to Washington Headquarters Services, Directorate for Information Operations and Reports, 1215 Jefferson Davis Highway, Suite 1204, Arlington VA 22202-4302. Respondents should be aware that notwithstanding any other provision of law, no person shall be subject to a penalty for failing to comply with a collection of information if it does not display a currently valid OMB control number.

1. REPORT DATE AUG 2011		2. REPORT TYPE		3. DATES COVERED 00-00-2011 to 00-00-2011	
4. TITLE AND SUBTITLE Flow structure and acoustics of supersonic jets from conical convergent-divergent nozzles				5a. CONTRACT NUMBER	
				5b. GRANT NUMBER	
				5c. PROGRAM ELEMENT NUMBER	
6. AUTHOR(S)				5d. PROJECT NUMBER	
				5e. TASK NUMBER	
				5f. WORK UNIT NUMBER	
7. PERFORMING ORGANIZATION NAME(S) AND ADDRESS(ES) Naval Research Laboratory, Washington, DC, 20375				8. PERFORMING ORGANIZATION REPORT NUMBER	
9. SPONSORING/MONITORING AGENCY NAME(S) AND ADDRESS(ES)				10. SPONSOR/MONITOR'S ACRONYM(S)	
				11. SPONSOR/MONITOR'S REPORT NUMBER(S)	
12. DISTRIBUTION/AVAILABILITY STATEMENT Approved for public release; distribution unlimited					
13. SUPPLEMENTARY NOTES					
14. ABSTRACT					
15. SUBJECT TERMS					
16. SECURITY CLASSIFICATION OF:			17. LIMITATION OF ABSTRACT	18. NUMBER OF PAGES	19a. NAME OF RESPONSIBLE PERSON
a. REPORT unclassified	b. ABSTRACT unclassified	c. THIS PAGE unclassified			

A convergent-divergent nozzle, whether conical or traditional, may be characterized by a design Mach number, M_d , which is the Mach number at the nozzle exit corresponding to the ratio of areas at the nozzle throat and nozzle exit by

$$\left(\frac{A_e}{A^*}\right)^2 = \frac{1}{M_d^2} \left[\frac{2}{\gamma+1} \left(1 + \frac{\gamma-1}{2} M_d^2 \right) \right]^{(\gamma+1)/(\gamma-1)},$$

where A^* and A_e are the throat and exit areas respectively and γ is the ratio of specific heats. Only sonic or supersonic solutions are of interest so, $M_d \geq 1$. The operating condition of an exhaust nozzle may be characterized by a jet Mach number, M_j , which corresponds to the pressure ratio between the total pressure supplied to the nozzle and the ambient static pressure outside the nozzle by

$$\frac{p_o}{p_\infty} = \left(1 + \frac{\gamma-1}{2} M_j^2 \right)^{\gamma/(\gamma-1)},$$

where p_o and p_∞ are the total pressure and ambient pressure, respectively, and γ is again the ratio of specific heats. The non-negative Mach number solution is used. The nozzle is then said to be overexpanded when $M_j < M_d$, on-design when $M_j = M_d$, and underexpanded when $M_j > M_d$.

A. Acoustics of shock-containing jets

The noise generated by shock-containing supersonic jets can be divided into three dominant components: screech, broadband shock-associated noise, and turbulent mixing noise. The turbulent mixing noise is not unique to supersonic jets and has been dealt with extensively in the literature of subsonic jets classically²⁻⁵ and more recently in terms of large-scale structure analysis.⁶⁻⁸

Broadband shock-associated noise may be identified by a spectral peak whose frequency is a function of the direction of radiation. The shock-associated noise peak frequency increases in the direction of the jet flow. The frequency dependence on the angle of observation was first explained as constructive interference of emissions from a phased array of correlated sources caused by large-scale structures passing through the regularly spaced shock diamonds.⁹ A mathematically more complete modeling of the large-scale structures in the shear layer reproduces the frequency dependence of the earlier theory, but also accounts for the broadening of the spectral peak with increasing inlet angle and the strong reduction in intensity of higher-order peaks.¹⁰ Broadband shock-associated noise is radiated most strongly in the upstream direction and grows stronger with $(M_d^2 - M_j^2)^2$ up to a maximum amplitude at the point at which Mach disks form in the jet.¹¹ The majority of broadband shock-associated noise has been found to occur in the middle¹² or in the later part¹³ of the region in which shock cells exist.

When first encountered, screech was observed to be caused by an interaction between shear layer turbulence and the shock waves in the jet.¹⁴ The near-field acoustic pressure distribution for screech has been shown to have a lobed character with regions of high intensity corresponding to the shock reflections from the shear layer.¹⁵ The upstream-running

waves in a screeching jet have been found to travel at the speed of sound and so it may be inferred that they are themselves acoustic waves.¹⁶ Later, the importance of instability and large-scale coherent structures in turbulence have been recognized. Instability waves interacting with the shock structure and with sound waves outside the jet have been shown to be essential to the generation of screech.¹⁷ The flow and the acoustics of circular and non-circular supersonic jets have been compared.¹⁸

The primary peak frequency of screech is never greater than the broadband shock-associated noise peak. In fact, it matches the primary peak frequency for broadband shock-associated noise for an observer directly upstream ($\psi = 0^\circ$). This observation has led to the theory that the broadband shock-associated noise is itself the mechanism of the upstream running portion of the feedback loop producing screech.¹⁹

Until the last few years, nearly all published results relating to shock noise from supersonic jets from C-D nozzles were obtained using traditional, smoothly contoured nozzles. The one exception reported far-field overall sound pressure level (OASPL) for a nozzle described as ‘‘an F15 nozzle’’ which showed elevated noise near the design condition as compared to a traditional C-D nozzle.²⁰ Recent interest in noise from military aircraft has motivated a number of studies of the acoustics of jets from the kinds of variable-geometry nozzles used on military jets. A high-fidelity nozzle with the facets associated with the flat panels and seals in a real engine nozzle has been tested and far-field acoustics presented in one-third octave bands with and without several noise reducing strategies.²¹

The design of the nozzle used by Martens and Haber²¹ was used by the present authors as a guide in designing the nozzle used in this study. Initial narrow-band far-field measurements revealed that the spectral features characteristic of screech and broadband shock-associated noise are present even at the design condition.²² Large Eddy Simulation (LES) by the present authors have shown the presence of shocks inside the conical C-D nozzle and the presence of shock diamonds even at the design condition.²³

Narrow-band spectra measured for the same nozzle revealed details of the spectral features of screech and broadband shock-associated noise.^{24,25}

The present paper expands upon the initial evidence presented by Munday *et al.*²² and Liu *et al.*²³ in improving the quality of the flow measurements with improved shadow-graph images and by adding Particle Image Velocimetry (PIV) data. The present paper also nearly doubles the domain over which near-field pressure fluctuations are measured and expands the number of operating conditions (M_j or NPR) over which far-field acoustic data is presented. The grid on which the LES has been performed has been further refined in the region around the nozzle exit to better resolve the shear layer and shock structures.

B. Experimental facility and procedure

The three conical C-D nozzles employed in this study are simplified static models of actual variable geometry nozzles. Rather building a laboratory model with variable

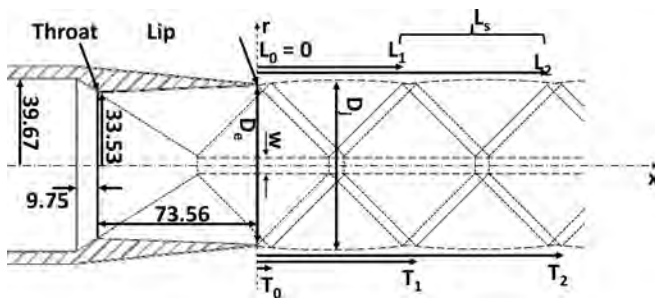


FIG. 1. Nozzle cross-section with schematic of a double-diamond shock cell structure. Dimensions shown are in millimeters. The three nozzles examined have values of D_e of 69.29, 72.85, and 76.35 mm.

geometry, three static CCD nozzles have been produced that approximate the real engine nozzles in three different configurations corresponding to three different operating conditions. The laboratory model cross-sections are circular rather than polyhedral so the surfaces of the convergent and divergent sections are conical. There are no hinges at the throat, but the sharp character of the throat is retained. The geometry of the nozzles is shown in Figure 1. All three nozzles are identical upstream of the throat. They all have a throat diameter, D_t , of 72.84 mm and expansion sections 73.56 mm in axial length. They have exit diameters, D_e , of 69.29, 72.85, and 76.35 mm giving the nozzles area ratios of 1.067, 1.181, and 1.295 and design Mach numbers, M_d , of 1.3, 1.5, and 1.65, respectively. The models are mounted in the University of Cincinnati Acoustic Test Facility (UC-ATF) which is a $7.32 \times 7.62 \times 3.35$ m test chamber which has been acoustically treated to be anechoic down to 500 Hz. This chamber includes fixtures for far-field acoustics and PIV flow measurements.

C. Experimental and numerical test conditions

Three experimental nozzles are used having design Mach numbers, $M_d = 1.3, 1.5,$ and 1.65 . Each nozzle was operated at multiple nozzle pressure ratios (NPRs) representing underexpanded, design condition, and overexpanded conditions. All cases were run with an unheated total temperature ($T_0 = 300$ K).

LES results presented here correspond to the underexpanded jet condition with the geometry corresponding to the $M_d = 1.5$ nozzle with total temperature $T_0 = 300$ K.

The nozzle pressure ratios used, the corresponding fully expanded jet Mach numbers, M_j , and other parameters of interest are shown in Table I. The Reynolds number, Re_j , is based on U_j and D_j , where U_j is the jet velocity and D_j is the fully expanded jet diameter. β_d is a shock strength parameter defined as $\pm (M_j^2 - M_d^2)^{0.5}$ where the plus sign is taken for underexpanded cases when M_j is greater than M_d , and the minus sign is taken for overexpanded cases when M_j is less than M_d . This parameter reduces to the β introduced by Harper-Bourne and Fischer⁹ for convergent nozzles where $M_d = 1.0$.

D. Instrumentation

The high gradient features in the flow are visualized by the shadowgraph technique. An Oriel 66056 arc lamp is used

TABLE I. Test conditions.

M_d	NPR	M_j	T_0 [K]	U_j [m/s]	D_j [mm]	Re_j [$\times 10^6$]	β_d
1.3	2.50	1.22	300	372.6	68.31	2.6	-0.44
1.3	2.77	1.30	300	390.1	69.24	2.9	0.00
1.3	3.25	1.41	300	415.1	71.07	3.3	0.56
1.3	3.69	1.50	300	433.2	72.80	3.6	0.76
1.5	2.50	1.22	300	372.6	68.31	2.6	-0.87
1.5	3.00	1.36	300	402.9	70.10	3.1	-0.64
1.5	3.50	1.47	300	425.8	72.05	3.5	-0.31
1.5	3.67	1.50	300	432.5	72.72	3.6	0.00
1.5	4.00	1.56	300	444.0	74.01	3.9	0.42
1.5	4.50	1.64	300	458.8	75.93	4.2	0.66
1.5	5.00	1.71	300	471.3	77.79	4.6	0.82
1.65	3.30	1.43	300	417.4	71.26	3.3	-0.83
1.65	4.59	1.65	300	461.2	76.27	4.3	0.00
1.65	6.30	1.86	300	496.5	82.32	5.5	0.86

for illumination. A pair of 305 mm parabolic first-surface mirrors with a 1.83 m focal length is employed to collimate the light before the model and then to refocus the beam after. The image is captured with an exposure time of $10 \mu\text{s}$ using a LaVision Imager Intense cross-correlation CCD camera with 1376×1040 pixel resolution and 12-bit intensity resolution. This gives a spatial resolution on the order of 0.004 throat diameters. A 28–300 zoom lens is mounted to the camera allowing optimization of the field of view. The aperture is left completely open and exposure is controlled by mounting a filter. Averaging 100 images eliminates the turbulence and gives a clear view of the shock and Prandtl-Meyer waves.

Detailed flow-field mapping is performed by PIV. The PIV system is built by LaVision and the entire PIV suite, laser and cameras are mounted on a traverse which allows the system to be translated, undisturbed, to any streamwise location allowing many fields of view to be measured without the loss of time in changing setups and without the uncertainties which come from repeated adjustment of components. The flow is seeded with olive oil droplets with diameters on the order of $1 \mu\text{m}$. A 500 mJ New Wave Research Nd:YAG double-pulse laser is passed through sheet-forming optics to illuminate the seed and the images are captured by a pair of LaVision CCD cameras with 1376×1040 pixel resolution and 12-bit intensity resolution. Images in each pair are separated in time by $1 \mu\text{s}$, giving peak particle displacements on the order of half a millimeter. The image scaling is 7.09 pixels/mm so the peak displacements are on the order of three pixels. The image pairs are cross correlated using a multi-pass method beginning with 64×64 pixel interrogation windows cascading down to 4×4 pixel windows with 0% overlap. The multi-pass method applies a window offset for each subsequent pass based on the results of the previous pass, improving accuracy. Assuming the displacement uncertainty of 0.04 pixels given in Ref. 26 gives an uncertainty in velocity of 5.6 m/s. This is on the order of $0.01U_j$. Individual velocity vectors above 550 m/s have been discarded as spurious. Discarded vectors are not replaced by interpolation in the final pass. Only valid vectors are considered for averaging or other statistical analysis. Histograms

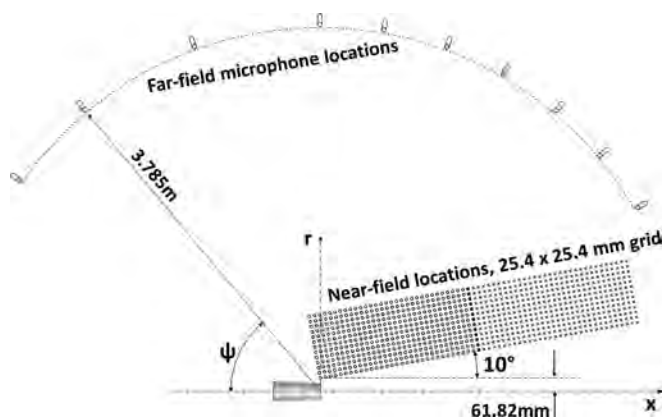


FIG. 2. Schematic of microphone locations for near-field and far-field measurements. The far-field array consists of 10 microphones ranging from $\psi = 35^\circ$ to 150° , each located 3.8 m from the center of the nozzle exit plane. The near-field array consists of a rake with 32 microphones which are traversed through 13 locations to sweep out a 0.3×0.8 m grid. Two such grids are swept to give a total region of 0.3×1.6 m.

of velocities in the individual vector fields have been checked and no evidence of pixel locking was found.

Far-field measurements are obtained by mounting B&K Type 4954-B quarter-inch free-field microphones on a circular arc 56 throat diameters from the center of the nozzle exit plane as shown in Figure 2. The facility is described in detail by Callender *et al.*²⁷ These microphones cover an arc between the angles 35° and 150° measured from the upstream direction. The microphone signals are low-pass filtered up to 100 kHz and recorded at 204.8 kHz for 10 s. The flow variables are monitored at 4 Hz in order to establish and hold the desired operating condition of the model. Variables recorded include the ambient conditions in the chamber as well as the stagnation temperature and pressure of the jet.

In order to map the near-field acoustics, thirty-two microphones are mounted at 2.54 cm intervals on a linear rake which is mounted on a large three-axis traverse and is then traversed radially outward by steps of 2.54 cm. This produces a grid of 31×12 measurement locations. Two 31×12 grids are taken to extend the overall region to 61×12 locations covering 23×4.5 throat diameters. One column of measurement locations is common to both grids. The location of the measurement grids are shown in Figure 2. The rake is angled at 10° to keep the microphones out of the flow as the jet spreads. The resulting grid of pressure fluctuations can then be analyzed on an Overall Sound Pressure Level (OASPL) basis or for particular frequencies pertinent to the different mechanisms and can be mapped to look at source location and direction of propagation.

Both far-field and near-field experimental acoustic data are analyzed in blocks of 4096 samples. Each block is windowed with a Kaiser filter and then a fast-Fourier-transform (FFT) is applied yielding narrow-band spectra with a frequency resolution of 50 Hz. After the spectra are nondimensionalized the spacing between Strouhal numbers is approximately 0.125. Finally the spectra derived from all the blocks are averaged. OASPL are determined from the time domain data by applying a 4th order high-pass Butterworth filter to remove content below 500 Hz, then determining the P_{rms} .

E. Numerical approach

The unsteady three-dimensional inviscid compressible flow equations are solved with a finite element code FEFLO on unstructured tetrahedral grids.²⁸ This code is capable of accurately representing complicated geometries, such as the nozzle geometries used in this work. The Flux-Corrected Transport (FCT) algorithm is used for the spatial discretization and a fourth-order Taylor-Galerkin scheme is used for the time integration. FCT is ideal for the shock containing flows because it is high-order, conservative, monotone, and positivity-preserving.²⁹ No explicit subgrid scale model is used and the modeling of subgrid scales is implicitly provided by the embedded flux limiter. The present simulations are in the category of monotonically integrated large eddy simulation (MILES) approach.³⁰

Characteristic boundary conditions are applied to both far field and outflow boundaries, and the total pressure is kept constant at the inlet of the nozzle. A slip boundary condition is applied to the nozzle wall, and no turbulence is added at the inflow boundary. The cell size is roughly $0.02 D_e$ near the nozzle exit and it gradually increases to $0.034 D_e$ in the wake region. Since the jets under study have Reynolds numbers greater than 10^6 , the shear layer near the nozzle lip is thin and a fine-mesh layer with a cell size of $0.0035 D_e$ is clustered near the nozzle lip and up to $0.5 D_e$ downstream to resolve the shear layer. The mesh size increases progressively and becomes very large in the far-field region. A buffer region is added near the far-field and outflow boundaries to avoid wave reflections. More details of the numerical approach and its validation can be found in Ref. 31.

After the flow field and the near-field acoustic fields reach a quasi-steady state, pressure information in the near field are collected at a small time interval ($< 0.04 D_e/U_j$), and a data set over a time length greater than $900 D_e/U_j$ is collected. This data set is divided into three blocks and each one has 8192 samples with a frequency resolution of 20 Hz. The final acoustic data are calculated by ensemble averaging data over all blocks. Both OASPL and the space-time correlations are evaluated over the entire data set and the near-field OASPL are evaluated from P_{rms} .

II. RESULTS AND DISCUSSION

A. Flow structure

LES reveals the flow inside the nozzle where it is difficult to make any unobtrusive flow measurements. Figure 3 shows mean Mach number contours inside the nozzle and in the region just past the nozzle exit for $M_d = 1.5$ and $M_j = 1.56$. The Mach contours reveal that the sharp throat produces an oblique shock inside the nozzle and forms a Mach disk near the centerline. For this case, the Mach disk lies at $x/D_e = -0.35$ which is inside the nozzle and the interface between the oblique shocks and the Mach disk casts a slip line near the jet centerline with a diameter of $r/D_e = 0.06$. The onward-running oblique shock extends from this internal Mach disk, past the nozzle exit and passes through the oblique shock anchored at the nozzle lip. It reflects from the shear layer outside the nozzle downstream from the nozzle lip at

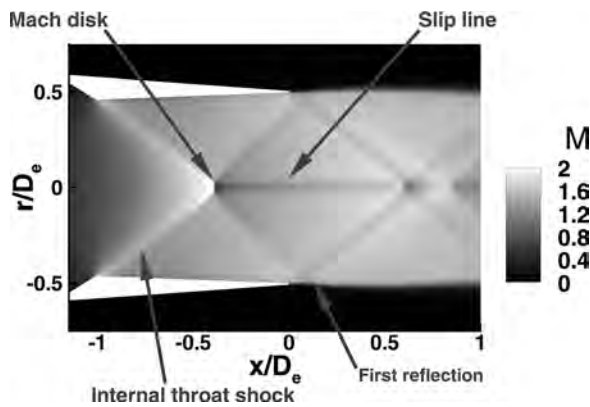


FIG. 3. Mean Mach numbers from LES inside the nozzle and near the exit for $M_d = 1.50$, $M_j = 1.56$.

$x/D_e = 0.07$. The wave reflected from this throat shock is an expansion wave that runs parallel to the lip wave towards the centerline.

The case shown in Figure 3 ($M_d = 1.5$, $M_j = 1.56$) is a mildly underexpanded case. The classical theory would suggest that overpressure will cause the flow to turn outward in an expansion fan which would be anchored at the nozzle lip and run inward toward the axis.³² Since this nozzle is conical, the flow exits with a radially outward component of velocity and must turn inward, despite the underexpanded condition, so the wave running inward from the lip is a shock. This can be seen by the drop in Mach number from the upstream side of the lip wave to the downstream side.

The flow pattern shown in Figure 3 differs from a classical supersonic jet in two ways, both due to the particular details of the nozzle. First, the conical expansion forces an inward turning of the flow near the nozzle lip for all cases near the design condition. The flow leaves the nozzle with an outward radial component of velocity and this must turn inward. Secondly, the sharp throat generates an oblique shock regardless of the condition outside the nozzle. The combined result of these two factors is that there are two overlapping

sets of shock diamonds produced and, as will be shown, these double diamonds are present for the design condition as well as for underexpanded and overexpanded conditions. This double-diamond feature is depicted schematically in Figure 1.

In Figure 4 shadowgraph and PIV results are compared. The case is $M_d = 1.5$ and $M_j = 1.56$. Instantaneous and averaged shadowgraphs are shown in Figs. 4(a) and 4(b), respectively. Instantaneous and averaged axial velocities from PIV are shown in Figs. 4(c) and 4(d).

Figure 4(a) shows an instantaneous shadowgraph image of the jet taken with an exposure time of $10 \mu\text{s}$. The turbulence near the nozzle appears fine grained, but the scale of the turbulence increases in the downstream direction. The outer edges of the jet are ragged with large scale structures and as these convect they produce Mach wave radiation which can be seen propagating at a downstream angle to the main jet. Oblique shocks can be seen emerging from the nozzle exit and reflecting from the shear layer at $x/D_e = T_0/D_e = 0.07$, where T_0 is the axial position of the reflected throat wave as shown in Figure 1.

These reflections make bright spots in the shadowgraph at the upper and lower shear layers and a bright vertical line connecting these spots. This is due to the integration along the line of sight. The jet geometry is axisymmetric and so are the oblique shocks and their reflections. The bright spots at the top and bottom of the image are reflections viewed in profile. Where the bright line crosses the jet centerline the camera is viewing the reflection through the near and far edges of the jet. The reflection of the shock is outside the field of view of the PIV images, but can be compared with LES Mach number contours in Figure 3. The LES image is a section in an axial plane and is not line integrated. The reflection of the throat shock is clearly visible in Figure 3 but the vertical line is not present since its origin is not in the plane computed by the LES.

The first complete double diamond can be seen in Figure 4(a), but as the turbulence is more pronounced farther downstream, the second cell is largely obscured. In order to reveal

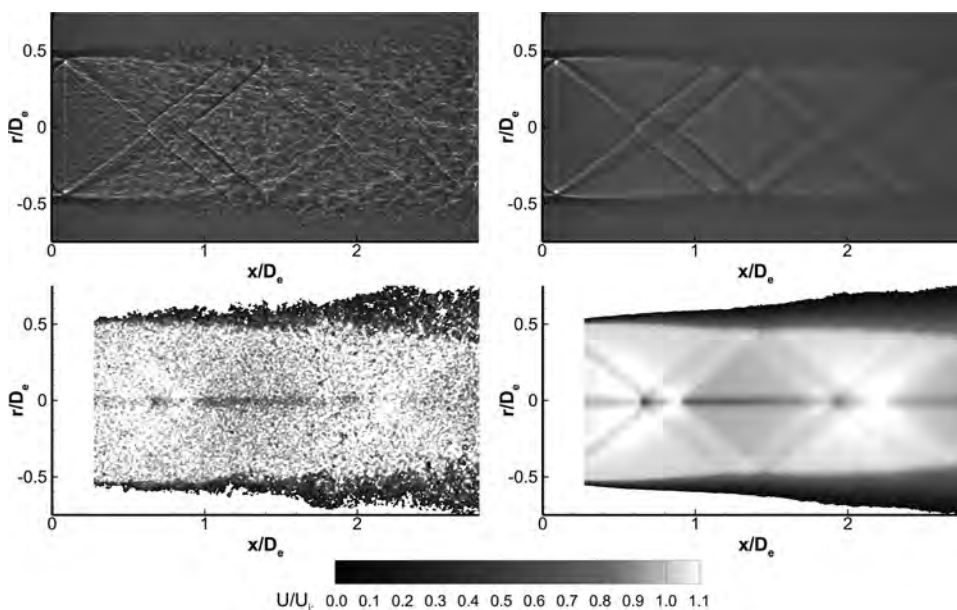


FIG. 4. Flow field representations by shadowgraph and PIV; $M_j = 1.56$, $M_d = 1.50$. (a) Instantaneous shadowgraph. (b) Average of 100 shadowgraph images. (c) Instantaneous PIV. (d) Average of 500 PIV image pairs. PIV velocities below $0.1 u/U_j$ are not shown.

the relatively stationary shock cell structures, 100 shadowgraph images were averaged. This process averages out the turbulence and leaves the shock structures visible. The averaged shadowgraph image is shown in Figure 4(b). In addition to the throat shock emerging from the nozzle and the first cell of the double diamond, the averaging brings out the reflection of the lip shock at $L_1/D_e = 1.1$ and the reflection of the throat shock at $T_1/D_e = 1.4$, and the next set of reflections at $L_2/D_e = 2.4$ and $T_2/D_e = 2.8$. L_n and T_n are the axial coordinates of the n th lip and throat wave reflections, respectively (see Figure 1). The shock structures become less sharply imaged as they get farther from the nozzle. This is due to the fact that they are not completely stationary. The shear layer is in motion as large-scale structures pass along it. Each reflection of a wave off the shear layer is reflecting off a moving entity so the reflected waves are moved by the reflections. This effect is cumulative so as the number of reflections increases, the degree of motion of the shocks and expansion waves increases, and the averaged images of these moving waves become increasingly smeared with each wave reflection.

Another feature revealed by the averaging of the shadowgraph images in Figure 4(b) is the slip line cast from the Mach disk inside the nozzle. This appears as a dark horizontal feature running along the centerline of the jet images. The width of the slip line, w , is the same as the diameter of the internal Mach disk. The presence of the slip line in the shadowgraph, and PIV to follow, provides confirmation of the presence of the Mach disk predicted by the LES in Figure 3.

The bright vertical line associated with the throat wave reflection at T_0 observed in the instantaneous shadowgraph image is present in the averaged image as well. The averaging out of the turbulence reveals similar, though less sharp vertical lines associated with the reflections at L_1 , T_1 , L_2 , and T_2 also. As previously discussed, these are artifacts of the fact that the shadowgraph image is a line integrating result. Comparing these features in the averaged shadowgraph in Fig. 4(b) with the corresponding averaged PIV in Fig. 4(d) shows that while the reflections are present, the vertical lines are not.

PIV in an axial plane is shown in Figures 4(c) and 4(d). A single instantaneous measurement from a single image pair is shown in Fig. 4(c) and an average of 500 such instantaneous measurements is shown in Fig. 4(d). While PIV has the benefit, relative to shadowgraph, of not being line integrating, it has a disadvantage in regions near a solid surface like the nozzle because light reflected from the hardware over-saturates the camera. For this reason the PIV domain begins near $x/D_e = 0.25$, away from the reflecting hardware. The plots shown are of the axial component of velocity and velocities below $u/U_j = 0.1$ have been omitted in order to mask the background noise.

The instantaneous measurement in c shows that the larger scale turbulence observed in the instantaneous shadowgraph is confined to the shear layer. In the shadowgraph one can see large scale turbulence over the entire jet because of line integration. PIV shows a cut through an axial plane and shows that the variation within the jet is small. There is large variation, however, in the shear layers. These are thin

at the nozzle exit and thicken significantly in the downstream direction. Large variation in velocity is apparent in the thickened shear layer as high-speed eddies entrain relatively still air from the jet's surroundings. Pockets of velocity below $u/U_j = 0.1$ (shown in white) are drawn deep into the shear layer.

The velocity differences across the shocks and expansion waves in the shock cells are small enough to be comparable to the random variation in velocity so the shock cells are not very pronounced in the instantaneous velocity plots. Averaging 500 measurements suppresses this variation and the mean velocity plot in Figure 4(d) clearly shows the double-diamond structure and the presence of the slip lines around the centerline. The initial reflection of the throat shock occurs outside the measurement domain, but all the remaining features previously observed are present.

As with the averaged shadowgraph, the first shocks are the sharpest in character. Later shocks become somewhat smeared since they fluctuate in location due to accumulated variation from additional reflections off the shear layer. The locations of the later waves should be understood to be average locations since the waves are in motion.

The wake of the internal Mach disk, bounded by two slip lines is evident throughout the measurement domain. The width of this slip line, w , was measured for all three nozzles and over a range of jet Mach numbers and it was found that it is chiefly a function of design Mach number. Increased M_d and increased area ratio lead to decreasing slip line width, and thus decreasing diameter of the internal Mach disk. The slip line width w/D_e is 0.09, 0.06, and 0.045 for M_d of 1.3, 1.5, and 1.65, respectively. There is also a very weak dependence on fully expanded jet Mach number, showing reduced w/D_e with increased M_j .

Comparison of Figure 4(d) with Figure 3 shows that the features associated with the double-diamond structure predicted by LES agree well with the PIV and shadowgraph. The shock and Prandtl-Meyer wave locations and the position of the wake from the internal Mach disk match and the LES provides a much clearer image of these than the PIV.

The axial velocity comparison between PIV and LES is shown in Fig. 5, where the distributions along the centerline and along a line at $r/D_e = 0.25$ are presented. The shock-cell shape and location are in a very good agreement between these two predictions, and the difference of the shock-cell locations is within $0.04D_e$. The major difference between these two predictions is the magnitude of the velocity; PIV measurement is roughly 4.0% higher than that of the LES prediction away from the jet center.

Figure 6 shows shadowgraph images for a range of NPRs including two overexpanded conditions, the design condition and two underexpanded conditions. There are double-diamonds apparent in all the shadowgraph images including the design condition ($M_j = M_d = 1.5$). This shows that the CCD nozzles studied in this paper do not achieve a shock-free condition at the design condition. A shadowgraph movie was taken of the nozzle as the set-point was slowly varied through a range from $M_j = 1.22$ through $M_j = 1.71$ (NPR = 2.0 up to NPR = 5.0), including the points around $M_j = 1.5$ where quasi-1-D theory predicts perfect expansion. Careful

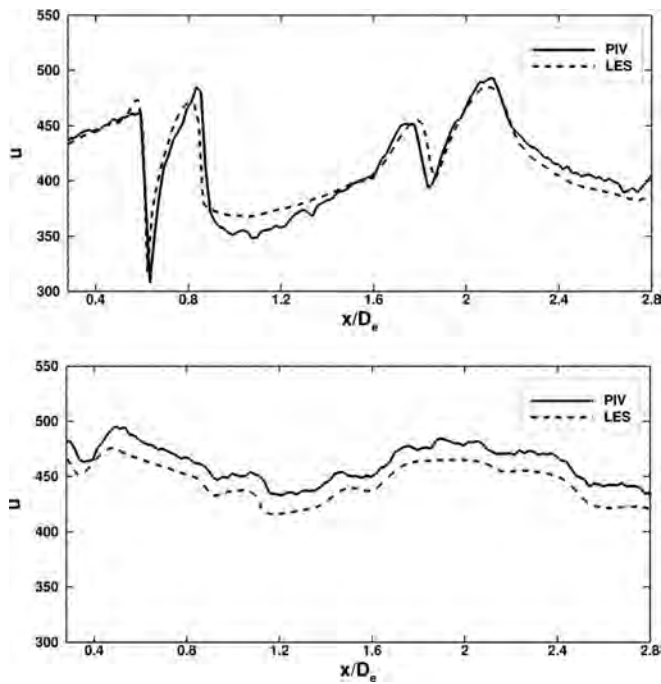


FIG. 5. PIV and LES velocities. $M_j = 1.56$ $M_d = 1.50$. (a) $r/D_e = 0$. (b) $r/D_e = 0.25$.

observation of the movie reveals that there is no condition in this range of M_j in which the jet is shock free.

For underexpanded conditions a decrease in M_j shortens the shock cells and also moves the two diamond structures closer to one another (L_i closer to T_i) until at the lowest condition the two sets of waves appear to have coalesced by the first lip wave reflection. By $M_j = 1.22$ the lip shock has formed a Mach disk three times the diameter of the internal Mach disk.

For overexpanded cases, increased M_j causes the reflections to grow closer to one another as the shock cells elongate. As the initial Prandtl-Meyer fan from the lip strengthens it becomes physically thicker and comes to envelop the throat waves entirely for the highest values of M_j .

One feature which is highly sensitive to M_d but relatively insensitive to M_j is the position of the initial throat wave reflection T_0 . For $M_d = 1.5$ it is 0.06 or $0.07 D_e$ for all cases except for $M_j = 1.22$ where T_0 is slightly closer to the exit ($0.04 D_e$). For the larger nozzle $M_d = 1.65$ the position of the initial throat reflection is farther from the nozzle at $T_0/D_e = 0.22, 0.29,$ and 0.32 for M_j of $1.43, 1.65,$ and 1.86 , respectively. The smaller nozzle, with $M_d = 1.3$, has the initial reflection of the throat wave inside the nozzle. Oil deposition within the nozzle observed after running reveals the location of the reflection to be at $T_0/D_e = -0.14$.

Figure 7 shows instantaneous static pressure distributions predicted by LES for a mildly underexpanded case ($M_d = 1.5, M_j = 1.56$). The high and low pressure regions alternating along the body of the jet mark the shock cells. Initially these clearly have an overall diamond shape. Beyond $x/D_e = 4$ or 5 the instantaneous images are less distinctly shaped and they begin to be shifted away from the jet centerline as the jet oscillates. By $x/D_e = 10$ or 12 the clear alternation of high and low pressures in the axial direction

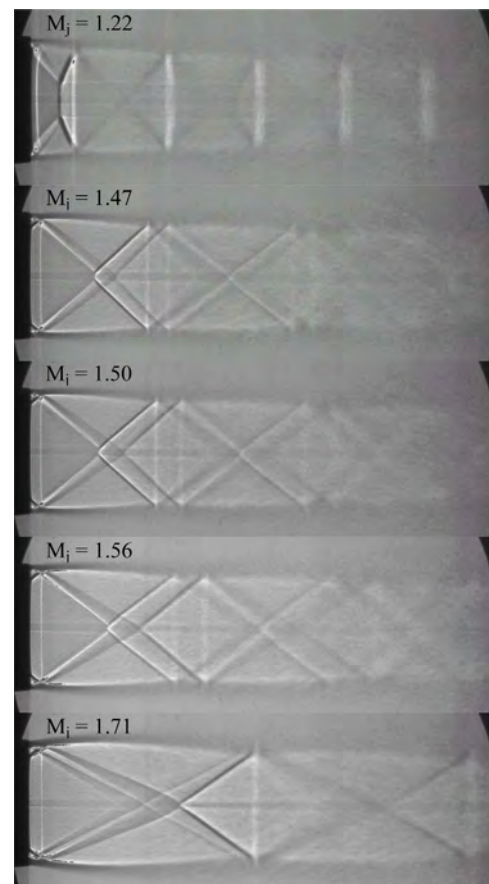


FIG. 6. (Color online) Convergent-divergent nozzle ($M_d = 1.5$) shadowgraph. One hundred images averaged to average out turbulence and emphasize shock structures.

ends. This marks the end of the potential core. Beyond this point the mixing has penetrated all the way to the jet center and the mixing process loses its cylindrical character.

Near the nozzle ($x/D_e = 0$ to 3) small pressure pockets can be seen along the edge of the jet. These are signatures of large-scale structures originating at the nozzle lip and connecting along the shear layer. They interact with the shock cells and grow larger as they move downstream. Beyond $x/D_e = 3$ they become comparable in size to the pressure pockets in the body of the jet caused by the shock cells.

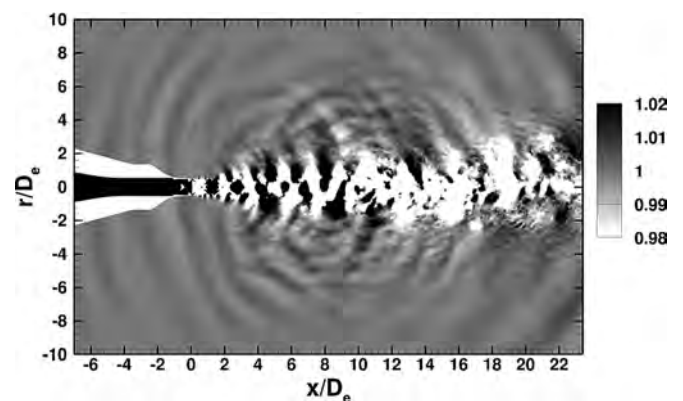


FIG. 7. Instantaneous pressure field from LES with jet condition of $M_d = 1.5, M_j = 1.56$.

Pressure waves with large intensities radiate from the region where the convecting large-scale structures have grown ($x/D_e > 3$) where the source is the vigorous interaction of the large-scale structures with the shock cells, producing screech and broadband shock-associated noises. Large pressure waves also radiate from the mixing region ($x/D_e > 10$) where mixing noise is the dominant feature.

Axial locations (L_i and T_i) of the reflections of both the lip waves and tip waves have been extracted from the PIV measurements. The throat and lip reflections are only distinguishable for the first two shock cells. Beyond this point the smearing due to shock motion blends the two. The shock cell spacing is nearly uniform over the first five cells. Beyond this the cells become shorter due to the thickening of the shear layer. This thickening reduces the diameter of the potential region and reduces the sonic diameter at which the reflections occur. Reducing the diameter of the cells also reduces their length. In order to give a single measure L_s of shock cell length, an average has been taken over the first five shock cells.

The shock cell spacing, L_s from PIV and LES is shown in Figure 8. Also shown are the theoretical values using the Prandtl-Pack relation,³³

$$L_s = \pi(M_j^2 - 1)^{1/2} D_j / \mu_1, \quad \text{where} \quad \mu_1 = 2.40483$$

as well as published data for a range of design Mach numbers from 1.0 to 2.0. Nearly all of the C-D nozzles previously published have been of the smoothly varying type, except in Seiner and Norum²⁰ and in Kuo, Veltin and McLaughlin²⁴ in which military style C-D nozzles were investigated. The Prandtl-Pack relation is generally a good fit for convergent nozzles ($M_d = 1.0$) depicted by small x 's. But it generally over-predicts L_s for higher values of M_d . This over-

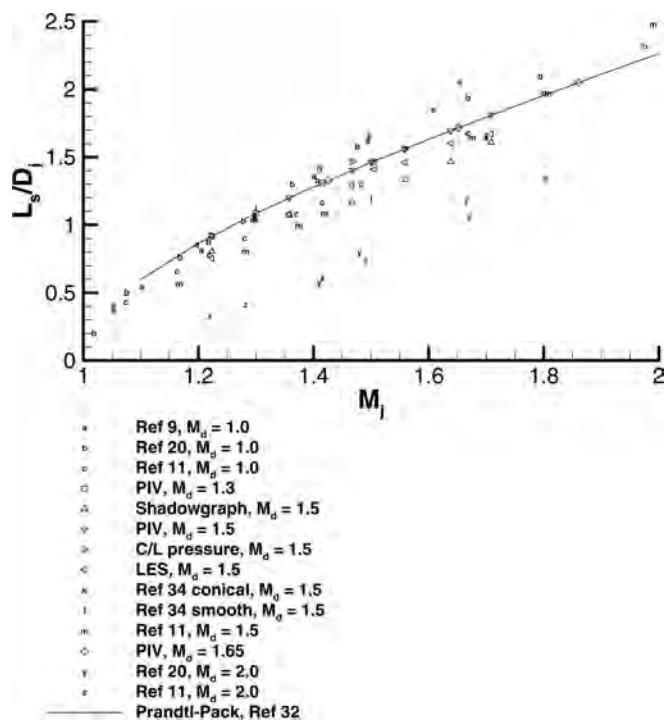


FIG. 8. Shock Cell size, L_s as a function of M_j .

prediction becomes worse as M_j increases. The general trend is that L_s increases with M_j , but for a given value of M_j the shock cell size decreases with M_d . The values of L_s extracted from PIV, from Shadowgraph, from centerline pressure measurements, and from LES all agree fairly well with one another and agree with other published results for nozzles with design Mach numbers near 1.5. It can be seen from this that there is not any significant difference in L_s introduced by the use of the more realistic CCD nozzles.

B. Acoustic emissions

Far-field acoustic spectra for the $M_d = 1.5$ nozzle are shown in Figure 9 for three conditions. $M_j = 1.47, 1.50,$ and 1.56 representing mildly overexpanded, design condition, and underexpanded. The frequencies are expressed in terms of a Strouhal number based on U_j and D_j . All three show signatures of shock associated noise. The narrow peak between $St = 0.2$ and 0.3 which radiates most strongly in the upstream direction ($\psi < 90^\circ$) is a screech peak and is as prominent at the design condition as the two off-design cases. All three sets also show the characteristic signature of broad-band shock-associated noise (BBSN). The BBSN peak is much broader than the screech peak, is centered at $St = 0.3$ or 0.4 at $\psi = 35^\circ$, and shifts to higher Strouhal numbers, grows broader, and lower as it shifts to more aft observers. By $\psi = 140^\circ$ the BBSN peak has shifted to $St = 1.1$ and is barely perceptible above the background mixing noise. At $\psi = 150^\circ$ the BBSN peak is negligible.

This similarity between the spectra of the design condition to those of off design conditions is characteristic of the conical C-D nozzles used in this study. Traditional smoothly varying C-D nozzles become shock free at their design condition, and therefore do not produce screech or BBSN at or near design condition. Operating a jet on-design can therefore offer significant reduction in noise for smoothly varying nozzles. For the practical engine nozzles used on high-performance jet aircraft this saving is not available even when the engine area ratio is closely matched to the operating condition.

Spectra for a far-field microphone at $\psi = 35^\circ$ are shown for all three nozzles as contour plots in Figure 10. The design condition for each nozzle is indicated by the horizontal black line. These plots were made by sweeping slowly through values of M_j so that any shock free spectra could be evident. No condition was found, however, for which there was no signature of shock noise. The dominant ridge in the plot is the screech tone. All three nozzles showed strong screech away from the design condition with a diminution in intensity and a frequency shift at the point at which the screech switched modes. The $M_d = 1.3$ nozzle shows two such shifts at $M_j = 1.25$ and 1.4 . The $M_d = 1.5$ and 1.65 nozzles only exhibit one such shift near the design condition. The broader and lower ridge to the right of the screech tone is the BBSN peak for each nozzle. This BBSN ridge is significant near the design condition for all three nozzles. There is a slight diminution in intensity for the $M_d = 1.3$ nozzle near $M_j = 1.4$ where the screech intensity is also at a minimum, but for the

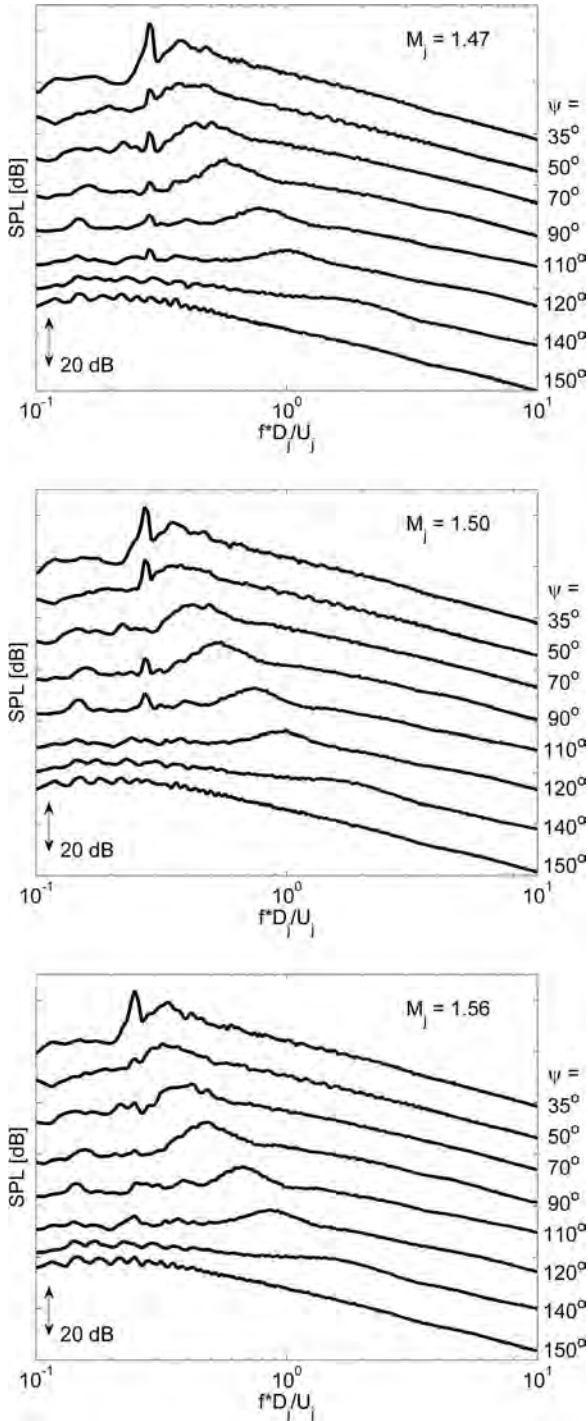


FIG. 9. Far-field acoustic measurements for the conical convergent-divergent nozzle with $M_d = 1.5$. Each trace is for a different angle, ψ , measured from the upstream direction. All measurements were taken at a distance of 56 throat diameters. (a) $M_j = 1.47$, overexpanded, (b) $M_j = 1.5$, perfectly expanded, and (c) $M_j = 1.56$, underexpanded.

$M_d = 1.5$ and 1.65 nozzles there is no reduction in BBSN whatsoever.

The peak frequency of the broadband shock associated noise is shown in Figure 11 for an observer at $\psi = 90^\circ$. These values are compared with published results for smoothly varying nozzles and for the military C-D nozzles tested by McLaughlen’s group.³⁴ The data for all nozzles collapse, whether smooth or conical, for all design Mach numbers.

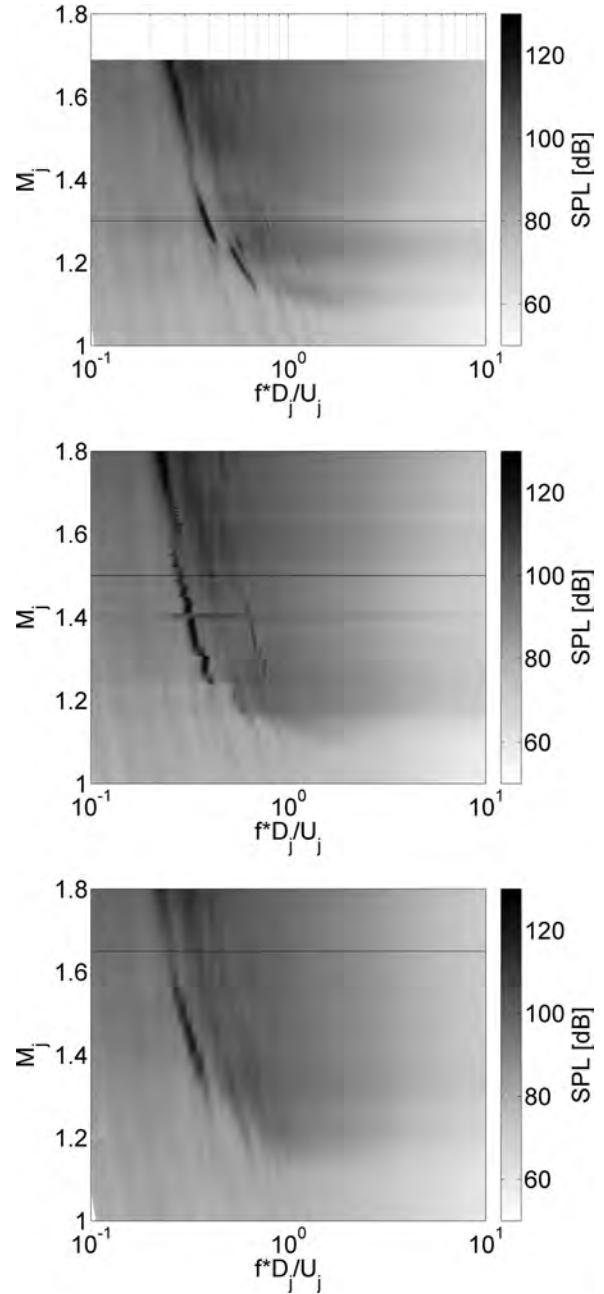


FIG. 10. Far-field spectra at $\psi = 35^\circ$. (a) $M_d = 1.3$. (b) $M_d = 1.5$. (c) $M_d = 1.65$.

There are also two theoretical curves due to Tam and Tanna.¹⁰ Equation of Tam and Tanna is based on a different derivation than Harper-Bourne and Fisher’s⁹ but the equation for the principal BBSN peak is the same,

$$f_p = \frac{U_c}{L_s(1 + \frac{U_c}{a_\infty} \cos \psi)},$$

where U_c the convective velocity is taken to be $0.7 U_j$. Tam’s derivation depends on knowledge of the shock cell spacing, L_s , for which he uses Prandtl-Pack’s equation above. The Tam-Prandtl-Pack line on the plot uses Prandtl-Pack for this. Tam-Shadowgraph uses the shock cell spacing read from the shadowgraph images in the present study. The

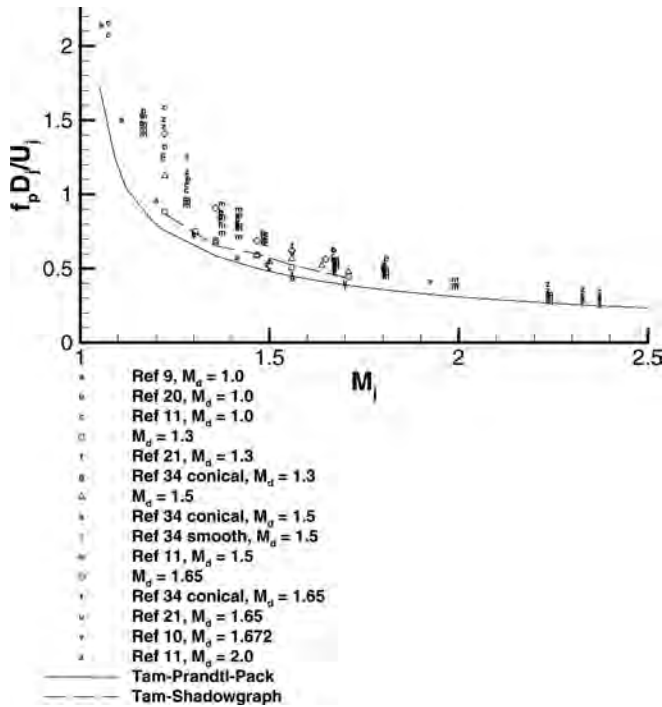


FIG. 11. Peak BBSN frequencies with varying M_j for an observer $\psi = 90^\circ$.

Tam-Prandtl-Pack equation under-predicts the BBSN frequency for nearly all cases, but correctly represents the trends. Substituting a measured value for L_s improves the Tam and Tanna equation considerably, but it remains on the low side. The trend in present measurements is for the BBSN frequency to rise with M_d especially at lower values of M_j .

Figure 12 shows a similar plot of screech frequency measurements, compared to published data and to theoretical curves expanded to predict screech. The agreement among

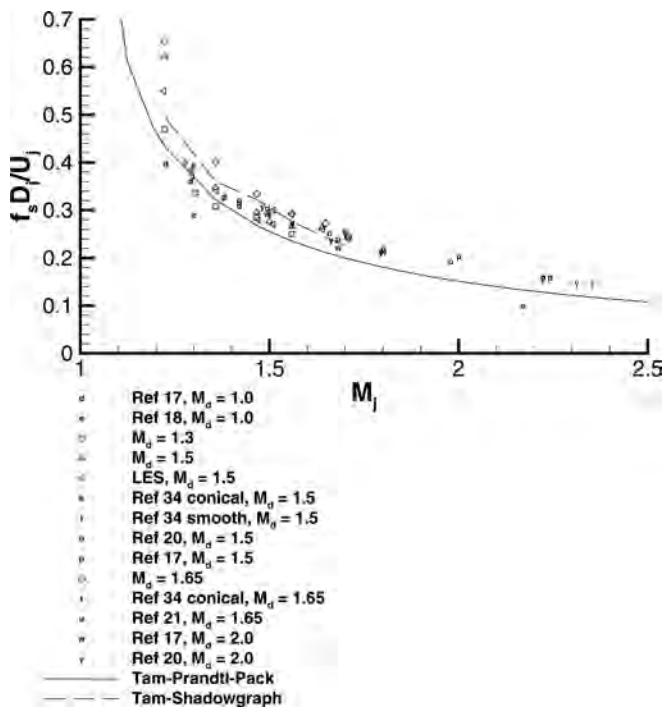


FIG. 12. Strouhal number of screech peak as a function of M_j .

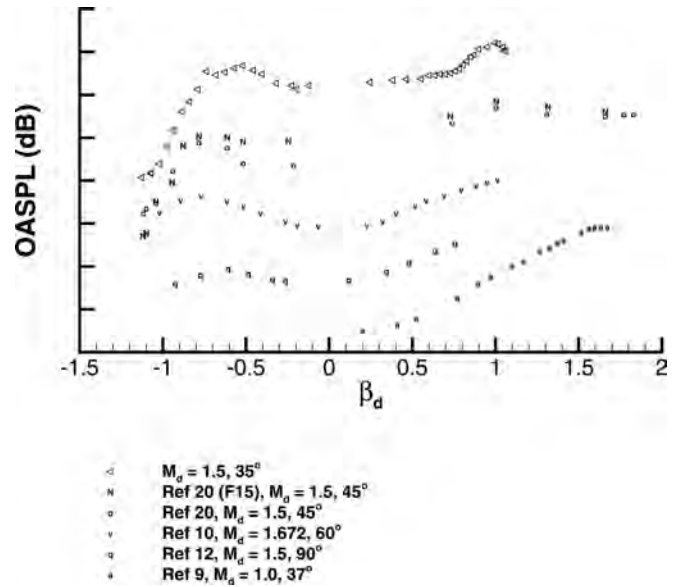


FIG. 13. Variation in OASPL with $\beta_d = \pm (|M_j^2 - M_d^2|)^{0.5}$.

different investigators is good, and the trend is for increasing Screech frequency with increasing design Mach number especially for lower values of M_j . Tam, Seiner, and Yu¹⁹ have proposed an explanation of the relationship between screech and BBSN which holds that the upstream propagating component of the screech feed-back loop is in fact the BBSN noise, and this the screech frequency will be the BBSN frequency as propagated to $\psi = 0^\circ$. As for the BBSN frequency, so the screech frequency is under-predicted by Tam-Prandtl-Pack, but is better with Tam-Shadowgraph. Screech is predicted by our LES and the agreement with experiment is good.

The CCD nozzles under study agree with smoothly varying nozzles in the frequencies of screech and BBSN, but the key difference acoustically is the presence of shock-associated noise near the design condition for conical C-D nozzles where it is absent for smoothly varying nozzles. Plots of OASPL as a function of β_d (Figure 13) show that there is a broad region of diminished OASPL around the design condition, but as discussed in Fig. 9 this is due to reduction in screech and there is no reduction in BBSN. Other published data co-plotted here show that for traditional C-D nozzles the reduction in OASPL near the design condition is more significant than the present study. Seiner and Norum²⁰ data of the ‘‘F15 nozzle’’ which is likely similar to the conical C-D nozzles shows similar trends to the present results.

C. Acoustic source locations

Contour plots of OASPL and Sound Pressure Level (SPL) for select Strouhal numbers are presented in Figure 14 for $M_d = 1.5$ and $M_j = 1.56$. Both measurement and LES results are shown. OASPL and SPL from LES occupy the rectangular region from $r/D_e = 0$ to 3 and $x/D_e = 0$ to 25 except for the region covered by near-field microphone measurements. The microphone data are shown in the rectangular region angled 10° from the jet axis and extending to $r/D_e = 9$

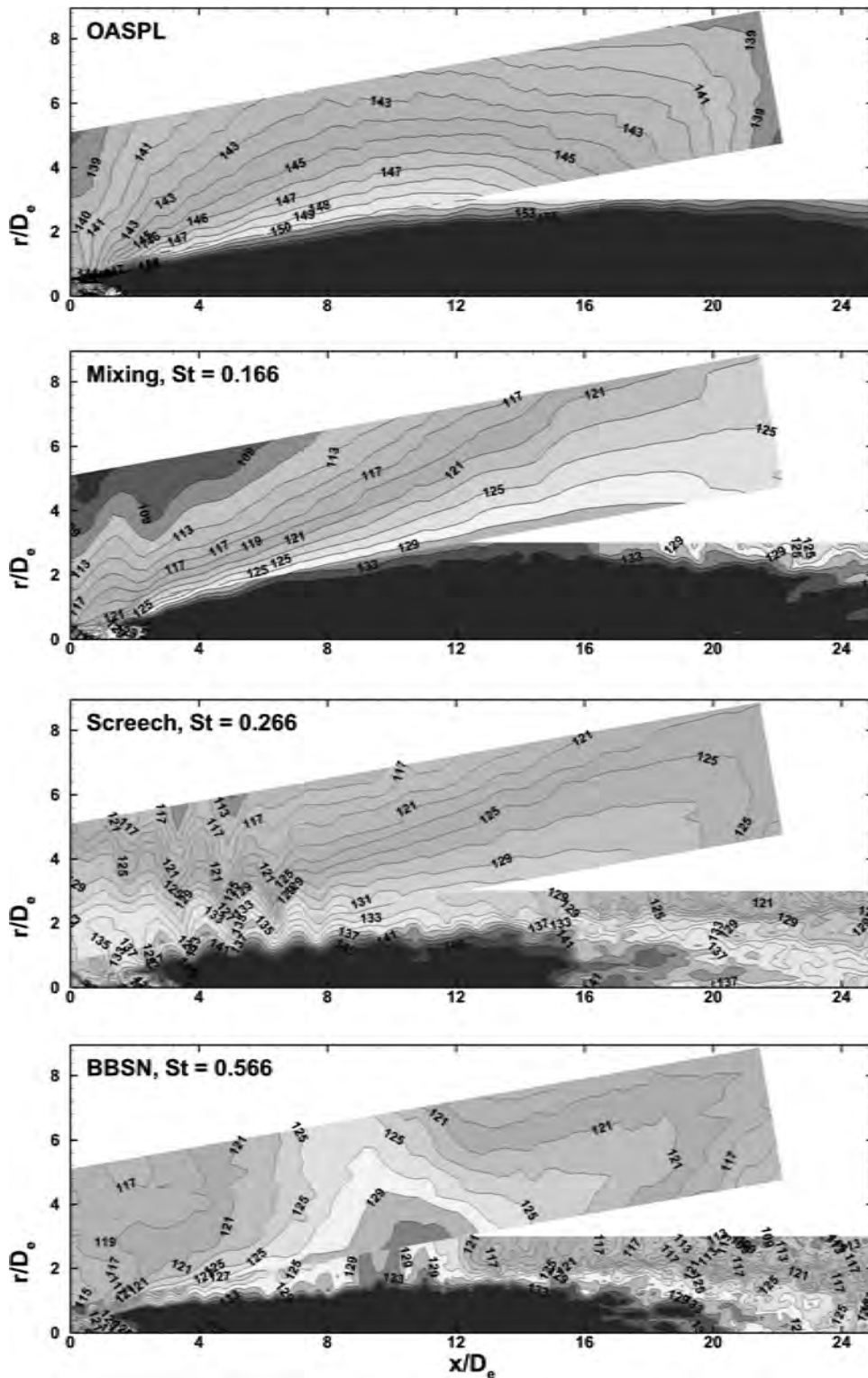


FIG. 14. Near-field contour maps of OASPL and 50 Hz bands for a slightly underexpanded case, $M_d = 1.50$, $M_j = 1.56$. Levels are in dB. (a) Over all sound pressure level. (b) Mixing noise, $St = 0.166$. (c) Screech, $St = 0.266$. (d) BBSN, $St = 0.566$.

and $x/D_e = 22$. When the two regions overlap, near-field measurement is shown.

Figure 14(a) shows the OASPL. First, note that the transition from LES to measurement is very smooth, except a very small region near the nozzle exit where the inflow turbulence dominates the pressure wave radiation. The jet is making noise across the entire length of the shock train. The maximum OASPL has an apparent source around $x/D_e = 10$, but high levels of OASPL range from $x/D_e = 2.5$ to 13. Sound pressure levels (SPLs) in 50 Hz bands around selected

frequencies are shown in the remaining subfigures. Figure 14(b) shows a Strouhal number of 0.166. This is in a frequency range below which no shock associated noise is generated, so it represents the mixing noise. Again a very good agreement is found between computations and measurement. Mixing noise appears to be radiating from the latter part of the shock train and extending beyond its end. Decibel levels above 130 appear ranging from $x/D_e = 7.5$ to 17.5. This apparent source region includes the region of intense mixing at the end of the jet's potential core. Figure 14(c) at a

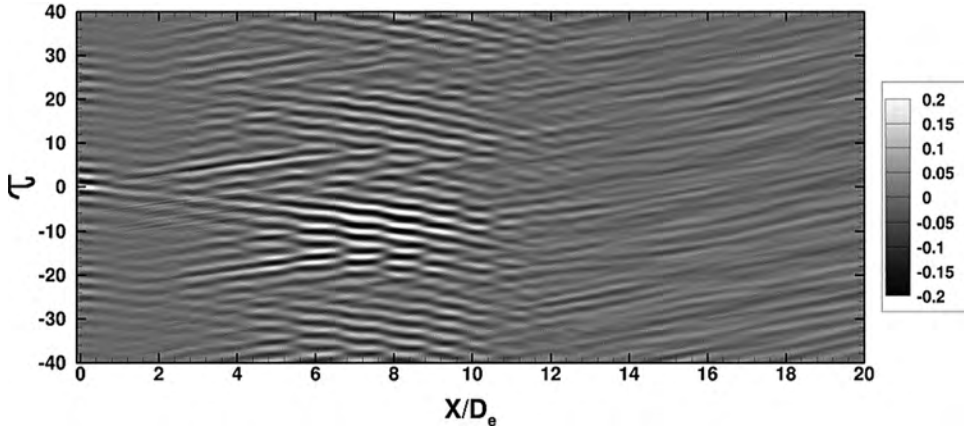


FIG. 15. Space-time fluctuating pressure correlations $\langle p'(0, 2D_e, \tau_0); p'(x, 0.5D_e, \tau_0 + \tau) \rangle / p'_{rms}{}^2$ between a reference point in the nozzle exit plane at two diameters and points along the lip line ($\tau = \text{time} \cdot D_e / a_\infty$).

Strouhal number of 0.266 is the screech frequency observed in the far-field. This plot shows the signature of screech in the form of a lobed source distribution with lobes centered on the shock reflections. The predictions of the lobe locations and the intensity agree with measurement well. Figure 14(d) at Strouhal number of 0.566 is based on the frequency of the BBSN peak observed in the far-field by an observer at $\psi = 90^\circ$. This distribution shows a single lobe centered on $x/D_e = 10.5$. This is the region where the large scale structures encounter the latter shock cells. For this frequency, the overall agreement between the measurement and LES predictions is good, but it appears LES under-predicts the intensity slightly.

Two-point correlations between fluctuating pressures in the near- and far-fields have been used to reveal source locations.³⁵ Since the LES in this case does not extend to the far-field, a reference point is chosen in the near-field. The reference point chosen is in the plane of the nozzle exit ($x/D_e = 0$) and well outside the jet ($r/D_e = 2$). This reference point is in the region in which the shock-associated components of jet noise are known to propagate. Figure 15 shows correlations of instantaneous pressure between the reference point and points along the lip line ($r/D_e = 0.5$) for a range of axial positions. The temporal delay τ ($\text{time} \cdot D_e / a_\infty$) is on the ordinate and x/D_e is on the abscissa. The peak correlation regions appear as streak lines with alternate positive and negative values in time, indicating that pressure fluctuations along the lip line with large correlation values are wave structures. From the upstream region to the location slightly downstream of the potential core, pressure fluctuations propagate in both downstream and upstream directions, as shown by the peak correlation lines that point towards both directions as the delay time decreases. However, the peak correlation lines only point to downstream in the mixing region, indicating that pressure fluctuations having large correlation values propagate downstream in this region. Although the pressure waves at the reference point correlate with pressure fluctuations along the lip-line over a large axial distance, the most intense region of correlation lies between x/D_e of 5 and 10 or roughly from the third shock cell to the end of the potential core. This region should be the major source location of the shock-associated noise. The frequency of the peak correlation lines pointing towards upstream is the same as that of the screech tone. This indicates that these peak corre-

lation regions directly reflect the correlation of the screech tone at the reference point with the pressure fluctuations on the lip line. In addition, since it is found that the averaged propagation velocity of these streak lines is around $0.8a_\infty$, the pressure waves at $5D_e \sim 10D_e$ on the lip line would take an amount of time with an average of roughly $10D_e/a_\infty$ to arrive at the nozzle exit. It can be seen that the pressure waves at the reference point are indeed strongly correlated with pressure fluctuations along the lip line from $5D_e$ - $10D_e$ with a delay time centered around $10D_e/a_\infty$. Furthermore, the pressure waves at the reference point are strongly correlated with the pressure fluctuations near the nozzle lip ($x = 0.0D_e$) at a later time. This is caused by the helical nature of the screech tone.

III. CONCLUSION AND SUMMARY

Conical C-D nozzles differ from traditional CD nozzles in two important respects, (1) that they have sharp throats and (2) that they diverge all the way to the exit creating an outward component of velocity in the exiting flow. These two differences each cause a series of shock diamonds to exist even when the nozzle is operated at perfect expansion, when $M_j = M_d$, and there is perfect pressure match at the exit. For all conditions, underexpanded and overexpanded as well as perfectly expanded, the presence of a sharp throat creates a second set of shock diamonds independent of the set produced by the nozzle exit producing a double diamond pattern.

The lengths of shock cells from conical C-D nozzles are not significantly different from those from traditional nozzles. The shock cell length is an important parameter in controlling the frequency of both broadband shock-associated noise and screech, so conical C-D nozzles produce peak frequencies similar to those of traditional C-D nozzles. The acoustic character distinctive to conical C-D nozzles is the presence of the shock-associated components of jet noise even when the nozzles are operated at perfect expansion. Both far-field and near-field acoustic measurements on conical C-D nozzles produce the same shock-associated noise signatures one would expect for a traditional C-D nozzle operated off-design. The only difference being that these signatures exist even at the design condition.

Agreement of the LES employed in this study with the measured quantities has been excellent. Suitably validated,

LES provides far greater detail than the measurements do and provides simultaneous and correlated results between pressure and velocity over the entire simulated domain while measurements of sound and flow fields are taken separately and are thus uncorrelated.

LES reveal the behavior inside the nozzle explaining the origin of the second set of shock diamonds and the central low-speed region in the wake of the internal Mach disk. Instantaneous LES provides a clear picture of the pressure pockets which mark the large-scale structures as they convect along the shear layer. The temporal pressure fluctuations caused by the passing of these pressure pockets are shown to be correlated with acoustic pressure fluctuations at a reference location outside the jet in the region through which shock associated noise is known to pass. The high correlation between the pressure fluctuations in the jet shear layer between 5 and 10 diameters with those at the reference location are convincing evidence that this is the source location for the shock-associated noise.

ACKNOWLEDGMENTS

This work has been sponsored by the Strategic Environmental Research and Development Program (SERDP). The authors gratefully thank Dr. Ravi Ramamurti from the Naval Research Laboratory and Professor Rainald Lohner from the George Mason University for their significant help with the computational code, FEFLO. They would also like to thank Dr. Steve Martens from GE Global Research for his guidance and advice in the design of realistic test cases and general insights into nozzle flow and acoustics.

- ¹T. Meyer, "Ueber zweidimensionale Bewegungsvorgaenge in einem Gas, das mit Ueberschallgeschwindigkeit stroemt," Ph.D. dissertation (Goettingen, 1908).
- ²M. J. Lighthill, "On sound generated aerodynamically. I. General theory," *Proc. R. Soc. London, Ser. A* **211**(1107), 564 (1952).
- ³M. J. Lighthill, "On sound generated aerodynamically. 11. Turbulence as a source of sound," *Proc. R. Soc. London, Ser. A* **222**(1148), 1 (1954).
- ⁴J. E. Ffowcs Williams, "The noise from turbulence convected at high speed," *Philos. Trans. R. Soc. London, Ser. A* **255**(1061), 469 (1963).
- ⁵G. M. Lilley, "On the noise from jets. Noise mechanisms," AGARD Conf. Proc. **131**, 13.1 (1974).
- ⁶C. K. W. Tam, M. Golebiowski, and J. M. Seiner, "Two components of turbulent mixing noise from supersonic jets," AIAA Paper No. 96-1716, 1996.
- ⁷C. K. W. Tam, "Influence of nozzle geometry on the noise of high speed jets," *AIAA J.* **36**, 1396 (1998).
- ⁸C. K. W. Tam, K. Viswanathan, K. K. Ahuja, and J. Panda, "The sources of jet noise: Experimental evidence," *JFMA* **615**, 253 (2008).
- ⁹M. Harper-Bourne and M. J. Fisher, "The noise from shock waves in supersonic jets. Noise mechanisms," AGARD Conf. Proc. **131**, 11-1 (1974).
- ¹⁰C. K. W. Tam and H. K. Tanna, "Shock associated noise of supersonic jets from convergent-divergent nozzles," *J. Sound Vib.* **81**, 337 (1982).

- ¹¹T. D. Norum and J. M. Seiner, "Measurements of mean static pressure and far-field acoustics of shock-containing supersonic jets," NASA TM Paper No. 84521, 1982.
- ¹²J. C. Yu and D. S. Dosanjh, "Noise field of a supersonic Mach 1.5 cold model jet," *J. Acoust. Soc. Am.* **51**(5A), 1400 (1972).
- ¹³J. M. Seiner and J. C. Yu, "Acoustic near-field properties associated with broadband shock noise," *AIAA J.* **22**, 1207 (1984).
- ¹⁴A. Powell, "The noise of choked jets," *J. Acoust. Soc. Am.* **25**, 385 (1953).
- ¹⁵R. Westley and J. H. Woolley, "The near field sound pressures of a choked jet when oscillating in the spinning mode," AIAA Paper No. 75-479, 1975.
- ¹⁶R. Westley and J. H. Woolley, "The nearfield sound pressures of a choked jet during a screech cycle," AGARD CP Paper No. 42 23: 113, 1969.
- ¹⁷J. C. Yu and J. M. Seiner, "Nearfield observations of tones generated from supersonic jet flows," AIAA 8th Aeroacoustics Conference, Atlanta Georgia, 11–13 April 1983, AIAA Paper No. 83-0706.
- ¹⁸E. Gutmark, K. C. Shadow, K. J. Wilson, and C. J. Bicker, "Acoustic radiation and flow instabilities in low supersonic circular and elliptic jets," AIAA Paper No. 87-2696, 1987.
- ¹⁹C. K. W. Tam, J. M. Seiner, and J. C. Yu, "Proposed relationship between broadband shock associated noise and screech tones," *J. Sound Vib.* **110**, 309 (1986).
- ²⁰J. M. Seiner and T. D. Norum, "Experiments of shock associated noise on supersonic jets," 12th AIAA Fluid and Plasma Dynamics Conference, Williamsburg, VA, 23–24 July 1979, AIAA Paper No. 79-1526.
- ²¹S. Martens and L. Haber, "Jet noise reduction for high speed exhaust systems," Proceedings of ASME Turbo Expo 2008: Power for Land, Sea, and Air, Berlin, Germany, 9–13 June, 2008, GT2008-50455.
- ²²D. Munday, E. Gutmark, J. Liu, and K. Kailasanath, "Flow and acoustic radiation from realistic tactical jet C-D nozzles," Proceedings of the 14th AIAA/CEAS Aeroacoustics Conference, Vancouver, British Columbia, 5–7 May 2008, AIAA Paper No. 2008-2838.
- ²³J. Liu, K. Kailasanath, D. Munday, E. Gutmark, and R. Lohner, "Large-Eddy simulations of a supersonic jet and its near-field acoustic properties," *AIAA J.* **47**, 1849 (2009).
- ²⁴C.-W. Kuo, J. Veltin, and D. McLaughlin, "Advanced acoustic assessment of small-scale military-style nozzles with chevrons," AIAA Paper No. 2010-3923, 2010.
- ²⁵D. McLaughlin, J. Bridges, and C.-W. Kuo, "On the scaling of small, heat simulated jet noise measurements to moderate size exhaust jets," AIAA Paper No. 2010-3956, 2010.
- ²⁶J. Westerweel, D. Dabiri, and M. Gharib, "The effect of a discrete window offset on the accuracy of cross-correlation analysis of digital PIV recordings," *Exp. Fluids* **23**, 20 (1997).
- ²⁷B. Callender, E. Gutmark, and R. Dimicco, "The design and validation of a coaxial nozzle acoustic test facility," AIAA Paper No. 2002-369, 2002.
- ²⁸R. Lohner, "FEM-FCT: Combining unstructured grids with high resolution," *Commun. Appl. Numer. Methods* **4**, 717 (1988).
- ²⁹J. P. Boris and D. L. Book, "Flux-corrected transport. I: SHASTA a fluid transport algorithm that works," *J. Comput. Phys.* **11**, 38 (1973).
- ³⁰F. F. Grinstein and C. Fureby, "On monotonically integrated large Eddy simulation of turbulent flows based on FCT algorithms," in *Flux-Corrected Transport: Principles, Algorithms, and Applications*, edited by D. Kuzmin, R. Lohner, and S. Turek (Springer, Berlin, 2005), Chap. III, pp. 79–104.
- ³¹J. Liu, K. Kailasanath, R. Ramamurti, D. Munday, E. Gutmark, and R. Lohner, "Large-Eddy simulations of a supersonic jet and its near-field acoustic properties," *AIAA J.* **47**, 1849 (2009).
- ³²H. W. Liepmann and A. Roshko, *Elements of Gasdynamics* (Wiley, New York, 1957).
- ³³D. C. Pack, "A note on Prandtl's formula for the wavelength of a supersonic gas jet," *Q. J. Mech. Appl. Math.* **3**, 173 (1950).
- ³⁴D. McLaughlin, private communication (2010).
- ³⁵J. Panda, R. G. Seasholtz, and K. A. Elam, "Investigation of noise sources in high-speed jets via correlation measurements," *JFMA* **537**, 349 (2005).